Effects of Coupling Multiple Factors on $CaCO_3$ Fouling in Agricultural Saline Water Distribution Systems

Tahir Muhammad[a,1], Yang Xiao[a,1], Jaume Puig-Bargués[b], Wenchao Liu[a], Zeyuan Liu[a], Xiuzhi Chen[a], Yunkai Li[a,*1]

a College of Water Resources and Civil Engineering, China Agricultural University, Beijing 100083, China

b Department of Chemical and Agricultural Engineering and Technology, University of Girona, Girona 17003, Spain.

*** Corresponding author.**

Yunkai Li

Tel: 86-10-62738485 E-mail: yunkai@cau.edu.cn

[1] Tahir Muhammad and Yang Xiao are co-first authors of this article.

Abstract: Saline water is an alternative resource that could be used to meet agriculture irrigation demands. Fouling, particularly that caused by calcium carbonate ($CaCO_3$), often occurs in saline irrigation water distribution systems, and severely restricts the utilization of saline irrigation water. So far, water acidification is the common practice for avoiding $CaCO_3$ fouling. However, this approach is often ineffective and regularly contributes to environmental pollution. This study investigated an affective practice to overcome $CaCO_3$ fouling issues by regulating shear stress, temperature and ions in saline irrigation water irrigation systems. The effects of different near-wall shear stress at 0.05, 0.20, 0.40 and 0.60 Pa, coupling with temperature of 10, 20 30 and 40 ºC and cations Mg^{2+} and Fe^{3+} were analyzed. Results demonstrated that the $CaCO_3$ fouling rate was linearly increased at initial shear stress, while decreased at higher shear stress, and the highest fouling rate was observed at 0.40 Pa, ranging between 21.4%-80.3%. The coupling of temperature and cations with shear stress significantly ($p < 0.05$) affected the fouling growth rate at each shear stress. The differences in fouling rate (fitting curves slopes k >1) among different shear stress get larger with increasing temperature, while they decreased and increased with the addition of Mg^{2+} and Fe^{3+}, respectively, when compared with pure solution of $CaCO_3$. Refinement analysis showed the largest unit-cell volume and lattice parameter of calcite at shear stress of 0.40 Pa, resulting in a significant effect on distribution of fouling particle sizes and morphologies. Moreover, some anti-fouling measures were further proposed based on the formation behavior of $CaCO_3$ fouling. These findings might provide a new perspective to control $CaCO_3$ with potential implications for sustainable saline water management for irrigation.

Key words: Clogging; Near-wall shear stress; Temperature; Ions; Rietveld refinement

1. Introduction

Fresh water scarcity is the major constraint for global food security and sustainable development of human society. Agricultural irrigation accounts for 69% of global freshwater consumption (FAO, 2016), but its demand it is forecasted to increase by 19% till 2050 (Liu et al., 2020). Widespread saline water is an alternative resource that could fulfill agriculture irrigation demands (Zhang et al., 2019). However, the high concentrations of cations and anions present in saline water often produce fouling in saline irrigation water distribution systems (SIWDS) (Zhang et al., 2016). Calcium carbonate ($CaCO_3$) is a predominant fouling sediment that accounts for 52.4%-94.1% of total fouling in SIWDS (Li et al., 2019; Ma et al., 2020), leading to numerous deleterious issues, i.e. decrease the system hydraulic efficiency (Li et al., 2019), pipeline surface corrosion (Hasson et al., 2019), partial or complete clogging of irrigation emitters (Alsadaie et al., 2019), negative effects on crop yield production (Ngan and Habimana, 2020), as well as increases both capital and operational costs of irrigation systems (Zhou et al., 2017). So far, the $CaCO_3$ fouling in SIWDS is often prevented by strong acids injection to lower the water pH (Peragón et al., 2017). However, these applications brought severe drawbacks such as soil environmental hazards (Song et al., 2019), and crop yield reductions (Khoshravesh et al., 2018). Therefore, investigating an acceptable physical anti-fouling operating conditions in SIWDS are key challenges.

Recent studies began to characterize the hydrodynamic operating conditions, which play an important role in minimizing fouling on pipeline surfaces (Kaya et al., 2014). Shear stress is an important hydrodynamic operating condition with a direct effect on $CaCO_3$ fouling (Freeman et al., 1990; Jaffrin et al., 2004; Paz et al., 2012). Several studies have explored the influence of near-wall shear stress (Hou et al., 2020), duration and frequency of shear stress (Chan et al., 2011), and constant shear stress (Rochex et al., 2008; Cowle et al., 2019) on fouling. These studies have clearly demonstrated a significant correlation between the shear stress and fouling process. However, the latest research advancement have beenmainly focused on the characteristics of biofouling formation. The impacts of near-wall-shear stress on $CaCO_3$ fouling in SIWDS are still elusive. It is well understood that shear stress significantly alter the fouling growth (Helalizadeh et al., 2000), fouling nucleation mechanism (Yang et al., 2011), restructuring and breakage of agglomerates (Soos et al., 2008), and morphologies and sizes distribution of crystal (Sonwai, & Mackley, 2006). However, $CaCO_3$ fouling process is not only depending on shear stress, but fluid temperature and ionic composition also plays a critical role on fouling growth. Thus, fouling process is influenced by mass-transfer (Ca^{2+} and HCO_3^- ion) (Hasan et al., 2012), surface-integration (Pääkkönen et al 2012), and sometimes the combination of both (Wang et al., 2016). These experimental parameters should be operated together (Korchef, A. 2019) which is therefore essential to explicitly understand the fouling mechanism. Furthermore, the formation of $CaCO_3$ fouling is related to the unit-cell parameters, such as cell-volumes, crystal sizes, and lattice parameters (Zhang et al., 2015). The development of Rietveld refinement technique has made it possible to investigate the characteristics of crystal, which might expose the potential interaction mechanism of shear stress and $CaCO_3$ fouling.

Thus, consider the fouling behavior in SIWDS under actual field conditions, $CaCO_3$ fouling was cultured on drip irrigation pipelines under the conditions of different near-wall shear stress, temperature and ions. The objectives of this work were to (1) investigate the $CaCO_3$ fouling mechanism under different near-wall shear stresses and operating conditions (temperature and added ions); (2) determine the control threshold of near-wall shear stresses for mitigating $CaCO_3$ fouling; and (3) elucidate the impacts of near-wall shear stresses on the lattice parameters of $CaCO_3$ fouling and the potential action mechanisms of shear stresses.

2. Materials and methods

2.1 Shear stress and water source preparation

An experiment was conducted applying four types of near-wall shear stress (0.05, 0.20, 0.40 and 0.60 Pa), which were in the domain of laminar flow in SIWDS and were comparable with previous studies (Hou et al., 2020). The applied shear stress was coupled with water temperature (10, 20, 30 and 40 °C), and two types of cations (Fe^{3+} and Mg^{2+}). Accumulatively the experiment had a total of 48 treatments, being their specific arrangements summarized in Table S1.

The experiment of $CaCO_3$ fouling was carried out with an accelerated CO_2 dissolved technique. At first, the $CaCO_3$ solution was prepared by dissolving 3.0 g of solid $CaCO_3$ in 10 L of deionized water until no solids were lift in solution. CO_2 gas was continuously fed into the solution overnight until Ca^{2+}, CO_3^{2-}, HCO_3- were prepared. A total of three solutions were prepared i.e., pure solution of $CaCO_3$ (CC), $FeCl_3$ (FC) and $MgCl_2$ (MC). During the experiment, the concentrations of the solutions were maintained as 0.2 g/L, and pH at a steady state of 5.5-5.7. Hereafter, to avoid any possible effects of left-over solids in solutions that might act as seed material and might affect the $CaCO_3$ fouling, the solutions were filtered through a 0.22 μm membrane filter before being introduced to the test devices.

2.2 Shear stress apparatus configuration and operation

An accelerated scale method using an annular reactor (AR) device, previously developed by Hou et al. (2020), was used. A total of 48 identical AR devices were used for fouling. The AR consisted of water storage bucket, a peristaltic pump, latex tubes, and a simulator as depicted in Fig. 1. The detailed description of AR device dimensions and operating conditions are detailed in Table S2. The device was composed of two exterior and interior concentric rotating cylinders. The rotation speed of internal cylinder was controlled by a servo head pump, generating desired near-wall shear stress at the internal surface of exterior stationary cylinder. The share stress simulation methodology is briefly explained in Supplementary materials section 1.1. Applied temperatures were carefully controlled by putting the AR devices in temperature-controlled incubators. A total of 8 incubators were set up, and each incubator consisted of 6 ARs.

Every individual AR was equipped with 24 polyethylene (PE) slides (pieces of drip irrigation laterals used for irrigation water distribution in agriculture fields) having dimensions of 19 × 1 cm, which were fixed at internal surface of exterior cylinder. The physical characteristics of PE were measured as roughness surface (Sq) 145 nm ± 6.1 nm, maximum height (Sy) 1504 nm ± 15.3 nm, and specific surface area (Sdr) 0.18% ± 0.02%. Thereafter, the arrangement and fixation of PE slides against the interior surface were done as described by Hou et al. (2020). Peristaltic water pumps with latex tubes and 10.08 ml/min flow rate were used to gently feed the prepared water solution from buckets to AR devices, and recirculate to solution buckets. The temperature of solutions was checked on daily basis, using a thermometer (type: O-264WT; range: -10 -300 ºC; accuracy: 1 ºC between -10 and 100 ºC; manufacturer: Dretec, Japan). Meanwhile, AR operated

10 h per day (8:00 a.m. - 2:00 p.m., 3:00 p.m. - 7:00 p.m.), lasting the experiment 300 h (30 days). Samples were collected after every 50 h, by randomly selecting 3 PE slides, which were cut out from each AR.

#Fig. 1 approximately here#

2.3 Sampling and characterization methods

2.3.1 Fouling dry weight extraction

The three selected PE pieces from each device at every sampling event were taken to analyze the fouling dry weight. The collected samples were dried in an oven for 20 min at 60 ºC. A high precision electronic weight balance (accuracy 10^{-4} g) was used to weight the samples (with fouling substances on it). The pieces were then placed in zip-lock bags, and 20 mL of deionized water were added to detach the fouling substances using an ultrasonic cleaner (manufacturer: Chaowei; type: GVS-10L; working rate of power: 240 W; frequency: 60 Hz). Hereafter, the clean and dried PE pieces (without fouling substances on it) were weighed again, being the difference between two weights was characterized as fouling dry weight.

2.3.2 Fouling characterization and evaluation

At the end of experiment, the phase composition and structure of fouling particles were identified by X-ray diffractometry (XRD). The samples were vacuum-dried at -15 ºC and scanned using a X-ray diffractometer (manufacture: Bruker, Germany; type: D8-Advance). The basic test conditions of the test process were: voltage 40 kV, current 40 mA, Cu target, and wavelength λ = 1.5406 Å. The XRD patterns were recorded in the scanning range of 2θ = 15-80° using a small angular step of 2θ equal to 0.017° and a fixed counting time of 4 s. The obtained polycrystalline diffraction patterns were then ameliorated by Rietveld refinement using the General Structure Analysis System (GSAS) (Larson and Von Dreele, 1994) to calculate the composition distribution (unit-cell volume & lattice parameters) of the obtained crystals. Finally, the obtained XRD map was analyzed using the supporting Topas software (Bruker _AXS, 2009) to determine the relative proportions of composed $CaCO_3$ polymorphs.

2.3.3 Apparent morphology of fouling particles

The $CaCO_3$ fouling particles sizes and morphologies were examined using a scanning electron microscope (SEM) (manufacturer: Japan Jeol, model: JSM-6510A), at an operating voltage of 20 kV after sputtered gold film and magnification ranging from 400× to 15,000×. The aspect ratios of particles size distributions were obtained by analyzing a minimum of 100 particles, using Morphologi G2 (Malven) instrument and its software.

2.4 Statistical analysis

The statistical analyses were carried out using SPSS (ver. 22.0 IBM, USA). Paired T-test was applied to determine significant difference among pair of shear stress treatments (p. adjusted < 0.05). Linear regression and analysis of variance (ANOVA) were applied to quantify the effect of each single and coupling factors. Structural equation modeling analysis (SEMA) was performed using SPSS AMOS v.24 (AMOS, IBM, USA) to analyze the direct and indirect effect of applied shear stress, temperature, and ions, on content of calcite and aragonite, and fouling total dry weight.

3. Results and analysis

3.1 Effects of near-wall shear stress on fouling dry weight

Overall, the growth of $CaCO_3$ fouling under each operating condition was divided in three phase development: growth induction (nucleation) phase (0-50 h), rapid growth phase (50-200 h) and stability phase (200-300 h) (Fig. 2). The fouling growth augmented with increase of shear stress from 0.05-0.40 Pa, while it decreased at 0.60 Pa. As observed from Fig. 2, the highest fouling dry weight at 0.40 Pa ranged between 0.18-1.83 mg/cm^2, which was 71.3%-80.3%, 35.6%-56.3% and 21.4%-54.2% higher than 0.05, 0.20 and 0.60 Pa, respectively. Meanwhile, significant ($p < 0.05$) differences were found among all shear stress treatments at each temperature and ions (Table S4). The significance analysis (Table 1) showed that the coupling of shear stress with water temperature and ions significantly affected ($p < 0.05$) the fouling growth rate.

In order to estimate the coupling effect of temperature and ions on fouling growth at shear stress, linear correlations between 0.05 Pa and other shear stresses were performed (Fig. S1). Significant linear correlations ($R^2 > 0.65$; $p < 0.05$) were obtained at each temperature and ion. The increased temperature positively increased fouling growth rate characterized by the larger slopes (k >1) of the fitting curves (Table S5). For instance, k values at 0.40 Pa compared with 0.05 Pa at 10 ºC reached to 3.22-4.28, while these were increased to 3.93-4.96, 4.41-5.41 and 4.77-5.41, showing that the fouling rate was increased by 81.9%-86.3%, 73.1%-79.1% and 67.5%-79.1% at 20, 30 and 40 ºC, respectively. Similarly, the k variation among different ions was analyzed at each temperature. The k variation at 0.40 Pa in CC ranged from 3.89-5.40, while FC tend to slightly increase and reached 4.28-5.71, However, MC were found to comparatively declined the k values reached 3.22-4.77 at 10-40 ºC, respectively.

On other hand, the different shear stresses significantly affected the fouling growth rate at each temperature and ions (Table S6). The slope (k) of fouling growth rate increased with greater shear stress. Taking the example of k values at 40 ºC when compared with 10 ºC under 0.05 Pa reached 2.54-3.48, which were increased to 3.85-5.10, 3.56-5.23 and 4.27-6.23 with shear rates of 0.20, 0.40 and 0.60 Pa, respectively. Besides, the k values under different shear stress in FC varied noticeably, increasing from 3.48, 5.20, 5.28 and 6.24 for 0.05, 0.20, 0.40 and 0.60 Pa, respectively.

#Fig. 2 approximately here#

3.2 Effects of near-wall shear stress on fouling phase change

Fig 3 shows X-ray powder diffraction and Rietveld refinement patterns (obtained for the samples at the end point (300 h) of system operation) and the mineral component proportions. The X-ray results revealed that the calcite was the most stable phase under each treatment since it contributed as 81.6%-93.3%, while aragonite ranged between 12.4%-24.9%. The T-test analysis (Table S4) showed that the quantity of calcite and aragonite minerals were significantly ($p < 0.05$) different among different shear stress in each operating condition, except for aragonite between 0.2 and 0.4 Pa. Among the treatments, the maximum amount of calcite was obtained at 0.40 Pa, ranging between 0.02-1.54 mg/cm^2 and being 25.8%-75.9%, 35.1%-82.6%, and 4.7%-66.3%. higher than 0.05 Pa, 0.20 Pa and 0.60 Pa, respectively (Fig 3 d, e, f). The coupling of shear stress with temperature and ion types presented a significant effect ($p < 0.01$) on calcite growth (Table 1). The content of calcite showed linear increasing trend with increase of temperature at each shear stress. However, addition of ions obviously changed the growth of calcite at each shear rate. For instance, the lowest content of calcite at constant temperature (40 ºC) ranged between 0.20-1.06 mg/cm^2 and was obtained with MC (Fig 3 (e)), which was 12.7%-34.1%, and 32.7%-36.8% lower than that for CC and FC, respectively (Fig 3 (d, f)). Moreover, the content of aragonite in presence of MC increased considerably reaching 0.03-0.08 mg/cm^2 (Fig 3 (h)), which was 14.7%-66.1%, and 79.3%-77.9% higher than with CC and FC, respectively (Fig 3 (g, i)).

#Fig. 3 approximately here#

#Table. 1 approximately here#

3.3 $CaCO_3$ particles size and morphology evaluation

The variation of $CaCO_3$ fouling particles sizes and apparent morphologies were determined under each shear stress, in presence/absence of ions and at different temperatures. The average largest particle sizes across the treatments were obtained at 0.40 Pa, ranging between 1.35-7.45 µm (Fig. 4 (a, b, c)). The fouling particle sizes increased positively with higher temperatures. Considering a constant shear stress of 0.4 Pa, the largest crystals were found at 40 ºC sized 6.18, 1.39 and 6.67 µm for CC, MC and FC, respectively.

Fig. 5 shows the SEM images of $CaCO_3$ fouling particles obtained at 40 ºC (40 ºC were taken as example, the detailed SEM images at 10, 20 and 30 ºC are summarized in (Fig. S2). The SEM images clearly agreed with the XRD results, indicating that $CaCO_3$ particles typically contain dominant proportion of calcite and small quantity of aragonite. The apparent morphologies of $CaCO_3$ particles exhibited a certain difference with the different treatments. Those particles in CC and FC at initial shear stress (0.05 and 0.20 Pa) were the mixture of calcite (Fig. 5 (a, b)) and aragonite (Fig. 5 (i, j)), but with increasing of shear rates (0.40 & 0.60 Pa) pure crystals of calcite were typically obtained as large particles of euhedral pseudo hexagonal platelets exhibiting dense-tight-thick layers (Fig. 5 (c, d & k, l)). On other hand, a higher quantity of aragonite with a smaller mono-crystalline, loose and distorted morphologies was obtained in MC (Fig. 5 (e, f, g, h)).

#Fig. 4 approximately here#

#Fig. 5 approximately here#

3.4 Variation of crystal unit-cell and lattice parameters

The XRD Rietveld refinement analysis was performed to determine the variation in $CaCO_3$ crystals structure and sizes affected by shear stress, temperature and ions (Fig 6). The X-ray results showed that the two phases acquired of $CaCO_3$ fouling particles were calcite and aragonite. Therefore, Rietveld refinement analysis was performed with calcite space group of (*R-3C* (167)) and aragonite (*Pmcn* (62)) (Crystallography Open Database (COD)). The calcite unit-cell volume (*Cv*) was 367.47, and lattice parameters were a = 4.98 Å, b = 4.98 Å and c = 17.05 Å, aragonite were 227.03 Å; a = 4.96 Å, b = 7.96 Å and c = 5.741 Å.

Fig 6 shows that, the average R_{wp} 0.003-0.04, and x^2 values 0.13-0.43 were recorded for all samples. The unit-cell volume of calcite exhibited largest expansion patterns at 0.40 Pa. Whereas, it increased *Cv* by 3.57-9.73, 2.44-5.62 and 1.13-3.24, when compared to 0.05, 0.20 and 0.60 Pa, respectively. Meanwhile, lattice parameters at 0.40 Pa were also increased by *a axis* 0.001-0.003, 0.0009-0.001, and 0.0003-0.001 Å, *b axis* 0.0008-0.002, 0.0009-0.002, and 0.0004 -0.0008 Å and *c axis* 0.04-0.11, 0.02-0.07, and 0.008-0.04 Å compared to 0.05, 0.20 and 0.60 Pa, respectively. Calcite lattice parameters were found significantly ($p < 0.05$) different among different shear stress (Table S8). However, the *Cv*, and lattice parameters (a, b and c) of aragonite were almost kept unchanged and most of the treatments were found non-significantly ($p > 0.05$) different.

#Fig. 6 approximately here#

3.5 Structural equation modeling analysis (SEMA)

This study also performed structural equation modeling analysis (SEMA) to further validate the hypothesis (Fig. 7). Consistent with experiment results, shear stress showed the strongest direct effects on calcite growth ($\beta = 0.46$; $p < 0.01$) and presented weak correlation with aragonite ($\beta = 0.22$; $p < 0.05$). At same time, ions also showed the strongest correlation with both calcite and aragonite ($\beta = 0.53, 0.58$; $p < 0.01$). However, temperature was in a weak and non-significant correlation with calcite and aragonite ($\beta = 0.23, 0.06$; $p < 0.05$), respectively. Matching with results of coupling effect of shear stress with temperature and ion on fouling growth slope, the inter-correlation among these three factors was found significant. Finally, both calcite and aragonite directly affected the total weight of $CaCO_3$ fouling with a significant correlation ($\beta = 0.73, 0.27$; $p < 0.01$).

#Fig. 7 approximately here#

4. Discussion

4.1 Effects of different operating conditions on $CaCO_3$ fouling growth

A set of experiments were designed to systematically determine the influence of varying operating conditions i.e., near-wall shear stress, water temperature and ions on fouling growth in SIWDS. The obtained results demonstrated that the growth of $CaCO_3$ fouling significantly ($p < 0.05$) depended on shear stress, temperature and ions (Fig. 2). Some studies postulated that the higher shear stress (cross-section flow velocity) sometimes linearly increases (Andritsos et al., 1997), or decreases fouling growth rate (Crittenden et al., 2015; Lee et al., 2013). The $CaCO_3$ fouling is mainly controlled by mass-transfer, surface-integration, or both mechanisms (Mwaba et al., 2006). In this study, the effects of applied near-wall shear stress on $CaCO_3$ fouling presented a quadratic correlation ($R^2 > 0.90$, $p < 0.05$) for each temperature and ion types (Fig. S3). This indicated that the fouling growth rate was positively increased at initial shear stress from 0.05 to 0.40 Pa and then there was a remarkable transition from positive to negative at higher shear rate of 0.60 Pa. The highest fouling rate at each temperature was obtained when the near-wall shear stress and flow velocity were 0.40 Pa and 0.24 m/s, respectively (Fig. S3). Hereafter, the fouling rate was significantly decreased when the shear rate reached 0.60 Pa and flow velocity was 0.41 m/s. These observations indicated that $CaCO_3$ fouling process was likely the mass-transfer controlled before reaching 0.40 Pa, hereafter changed to activation-controlled at higher shear rate of 0.60 Pa. However, these results were quite different from those reported by Helalizadeh et al. (2000), who applied flow velocities between 0.5 and 2 m/s, and found that the fouling process was mass-transfer controlled when the flow velocity was between 0.40 and 0.80 m/s, Hereafter the mechanism was activation controlled when flow velocity increased to 0.80-1 m/s, which could be probably explained by the high temperature (50-90 ºC) and ions solution concentration (0.25-1 mg/L) applied in the experiment. Wang et al. (2016) applied a flow velocity range of 0.06-0.80 m/s, and explained this phenomenon as the laminar boundary layer was increased linearly until 0.06-0.30 m/s, increasing the fouling average growth rate. However, when velocity was increased above 0.30 m/s, the turbulence flow increased the shear stress on surface of pipeline and fouling removal rate, as well as shortened the fluid residence time at the wall surface, thus, reducing the probability of the depositing material to adhere to the surface (Pääkkönen et al., 2012).

The effects of different temperature on fouling growth demonstrated that the increase in temperature linearly increased $CaCO_3$ fouling growth. Similar results were reported by Hasan et al. (2012), who found the higher the solution temperature the lower the fouling resistance. They further explained that the wall temperature directly increases with the increase of solution temperature, which increases the supersaturation at wall surface. The increased wall temperature decreases the inverse-solubility of $CaCO_3$, increasing the supersaturation at the wall surface and eventually further leads to increase fouling rate (Wang et al., 2016). In addition, the Rietveld refinement analysis demonstrated significant expansion of unit-cell volume and lattice parameters of calcite with increase of temperature at each shear stress (Fig. 6). These results were also in a good agreement with previous reports (Chang et al., 2017).

Furthermore, the nature of $CaCO_3$ fouling growth was not obviously changed under FC but slightly increased the fouling rate when compared to CC. The growth of $CaCO_3$ fouling regardless of shear stress and temperature were significantly ($p < 0.05$) inhibited under MC when compared with CC and FC. However, MC strongly promoted the formation of aragonite at each shear stress and temperature. The effect of Mg^{2+} has been reported briefly by several authors (Martos et al., 2010; Rodriguez-Blanco et al., 2012), suggesting that the dehydration energy difference between Ca^{2+} and Mg^{2+} ion is responsible for the inhibition of the $CaCO_3$ precipitation. The Rietveld refinement of X-ray diffraction demonstrated that the lattice parameters of calcite were exclusively changed with added ions. Thus, lattice parameters of calcite were slightly increased in CC and FC. Ma et al. (2016) postulated this occurrence, as doped Ca^{2+} probably would be introduced to the host lattice of $CaCO_3$ crystal in CC or FC, thus causing the expansion of lattice parameters. However, lattice parameters in MC were comparatively lower than those in CC and FC. This was due to the substitution of the Ca^{2+} ions in $CaCO_3$ by the Mg^{2+} since the atomic ion radius of Mg^{2+} (1.598 Å) is smaller than that of Ca^{2+} (1.974 Å) (Mejri et al., 2014).

The XRD diffraction results and SEM images indicated that the $CaCO_3$ fouling was a mixture of calcite and aragonite minerals. However, with the exception of MC, calcite minerals were the predominant phase under each condition (Fig. 3). The total fouling particle size of calcite was positively increased with shear stress and temperature (Fig. 4). Furthermore, the calcite crystal cell-volume and lattice parameters showed obvious expansion with increase of particle size. Several previous studies have demonstrated the significant ($p < 0.05$) positive or negative correlation between crystal size and lattice parameters (Mhadhbi et al., 2010; Sheng et al., 2010). Our results were in strong agreement with results previously reported (Mhadhbi et al., 2010; Qi et al., 2005). The calcite crystals were tightly compact and smooth surfaces with very small quantity of aragonite particles was found at higher shear rates. According to Daoyin et al., (2018), the higher shear stress results in breakup of aggregates, since the stable size of aggregates decreases with increasing shear stress.

4.2 Coupling effects of temperature and ions on shear stress fouling

This study also investigated the coupling effects of water temperature and added ions on $CaCO_3$ fouling at different near-wall shear stress. The coupling of shear stress at each temperature demonstrated that the fouling rate was positively increased at initial shear stress, while decreased at higher shear stress rates. This could be attributed to increased convective heat transfer, where increasing flow velocity decrease the wall temperature. Pääkkönen et al. (2012) found that increased velocity from 0.20 to 0.40 m/s reduced the wall temperature by 15 ºC, which strongly describe the variation in fouling rate. On the other hand, the coupling of varied temperature at shear stress and added ions fouling rate demonstrated that the rise in temperature from 10-40 ºC, linearly increased $CaCO_3$ fouling growth (Table S5), which has been discussed earlier. Similarly, the coupling effects of added ions on fouling growth at each shear stress were estimated (Table S7). The coupling of shear stress with added ions indicated that the fouling growth rate was reduced by higher shear stresses. This was due to greater mass transfer boundary layer thickness at lower flow velocities, therefore molecular diffusion strongly affected fouling growth. However, the higher flow velocities decreased the boundary layer thickness and fouling process was changed from mass-transfer to reaction-controlled. Therefore, water temperature and ions addition are two important factors that should be taken into consideration when applying shear stress to alleviate $CaCO_3$ fouling.

4.3 Engineering implications for anti-fouling in SIWDS

This study clearly demonstrated that $CaCO_3$ fouling was significantly affected by near-wall shear stress under different operating conditions i.e., different temperature and ions. It is important to evaluate the engineering implications to further validate the results for successful application in SIWDS. The average thickness of $CaCO_3$ fouling reached its maximum at a shear stress of 0.40 Pa and at a velocity of 0.24 m/s, while the higher shear stress 0.60 Pa at 0.41 m/s decreased its growth rate. Previous studies (Li et al., 2015; Puig-Bargués and Lamm 2013) suggested that better sediments removal rate is achieved when flushing velocity was around 0.45 m/s. Considering these results, this study strongly recommends the shear stress equal or above 0.60 Pa should be maintained in SIWDS. In addition, the emitter complex labyrinth channels create discontinuity in flow velocity (Liu et al., 2016) and, consequently, create high-speed and low-speed flow zones, which significantly alter the solid particles deposition rate at inlet, mid and end parts of emitter flow channels (Xiao et al., 2020). We suggest a careful design to minimize the dead areas (regions that allow suspended particles to settle and deposit) in SIWDS and to avoid shear forces around 0.4 Pa on emitter surfaces. On other hand, the increasing temperature linearly increased the fouling growth rate. Therefore, evening irrigation events are recommended to the crop fields when using SIWDS particularly in summer season or in hot weather areas, Dong et al. (2016) reported that night drip irrigation decreased the soil shallow root zone temperature by 0.6 ºC, promoted plant height, and crop yield by 2 % and 10 %, respectively. Furthermore, the coupling of water temperature with shear stress demonstrated the higher shear stress promoted the convective heat transfer at each temperature thus reducing the rate of fouling growth. It is suggested the higher shear stress should be used in SIWDS during high temperature irrigation events. Our results also demonstrated that Fe^{3+} increased the fouling growth rate when compared with Mg^{2+}. The coupling of shear stress with ions indicated that, the higher shear stress reduced the boundary layer thickness in each added ion, which resulted in decrease of the fouling growth rate. Therefore, we suggest that, firstly, when using high saline irrigation water (which contains CO_3^{2-}, PO_4^{3-}, SO_4^{2-}, SiO_3^{2-}, OH^-, Fe^{3+}, Fe^{2+}, Mn^{2+}, Ca^{2+}, S^{2-}, etc.) application in SIWDS integrated with fertigation, particular attention should be paid to the concentration of foreign added ions through fertilizers. Secondly, the results demonstrated the calcite fouling was easier formed at 0.40 Pa, indicating that the shear stress should be maintained at 0.20 Pa or 0.60 Pa. However, due to the main function of an emitter is energy dissipation, if the shear stresses were controlled at less than 0.2 Pa, the flow in emitter channel would be almost in low-speed regions. In emitters with good energy dissipation, the lengths of emitter channels are mostly very long, the flow indexes are very high, hydraulic performance is comparatively reduced, and have higher manufacturing costs (Feng et al., 2018). Therefore, we recommend the higher flow velocity (shear stress ≥ 0.60 Pa) should be maintained in SIWDS synergistically improving the emitter hydraulic performance and alleviate the calcium carbonate precipitation.

In summary, the present experimental results pave the way for studies of various aspects of fouling, including, effect of near-wall shear stress, temperature gradients, and added ions on controlling of $CaCO_3$ fouling in SIWDS. The results suggested that higher shear stress could be effective in mitigating $CaCO_3$ fouling. Nonetheless the meaningful findings were acquired in this study to greater insight on near-wall shear stress in SIWDS, the issues of integrated application of saline irrigation and fertilizer in SIWDS, sufficient number of cations should be considered in future studies.

5. Conclusion

The main conclusions derived from the experiment carried out in the present study are:

1. Overall, the fouling growth rate under different near –wall shear stress shows significant ($p < 0.05$) differences under each operating condition of temperature and added ions. The highest fouling rate ranged between 0.30-1.83 mg/cm^2 and was observed at 0.40 Pa, which was 59.3%-80.3%, 37.6%-56.3%and 21.4%-50.2% higher than 0.05, 0.20 and 0.60 Pa, respectively.

2. Temperature and added ions significantly ($p < 0.01$) affected $CaCO_3$ fouling rate under each shear stress. The fouling growth fitting curves (k) slope difference between 0.40 and 0.05 Pa linearly increased with increase of temperature 20-40 ºC. Similarly, these slopes varied significantly with addition of ions, where FC tend to increase, while MC decline the fouling

growth slope when compared with CC.

3. The XRD and SEM observation revealed that the $CaCO_3$ fouling in CC and FC were predominantly caused by calcite minerals, while the content of aragonite became more stable in MC. Crystal apparent morphologies in FC exhibited as dense-tight-thick layered structure, and MC was observed with loosed and distorted structures.

Acknowledgements

The authors are grateful for financial support from the National Key Research Project (2017YFD0201504), the National Natural Science Foundation of China (51790531, 51621061). The authors also gratefully acknowledge the insightful comments and suggestions of all reviewers

References

Alsadaie, S., Mujtaba, I. M. 2019. Crystallization of calcium carbonate and magnesium hydroxide in the heat exchangers of once-through Multistage Flash (MSF-OT) desalination process. *Computers & Chemical Engineering*, 122, 293-305. https://doi.org/10.1016/j.compchemeng.2018.08.033.

Andritsos, N., Karabelas, A. J., Koutsoukos, P. G. 1997. Morphology and structure of $CaCO_3$ scale layers formed under isothermal flow conditions. *Langmuir,* 13(10), 2873-2879. https://doi.org/10.1021/la960960s.

Chan, C. C. V., Bérubé, P. R., Hall, E. R. 2011. Relationship between types of surface shear stress profiles and membrane fouling. *Water research*, 45(19), 6403-6416. https://doi.org/10.1016/j.watres.2011.09.031.

Chang, R., Choi, D., Kim, M. H., Park, Y. 2017. Tuning crystal polymorphisms and structural investigation of precipitated calcium carbonates for CO_2 mineralization. *ACS Sustainable Chemistry & Engineering*, 5(2), 1659-1667. https://doi.org/10.1021/acssuschemeng.6b02411.

Cowle, M. W., Webster, G., Babatunde, A. O., Bockelmann-Evans, B. N., Weightman, A. J. 2019. Impact of flow hydrodynamics and pipe material properties on biofilm development within drinking water systems. *Environmental technology*, 1-13. https://doi.org/10.1080/09593330.2019.1619844.

Crittenden, B. D., Yang, M., Dong, L., Hanson, R., Jones, J., Kundu, K., Harris, J., Klochok, O., Arsenyeva O., Kapustenko, P. 2015. Crystallization fouling with enhanced heat transfer surfaces. *Heat Transfer Engineering*, 36(7-8), 741-749. https://doi.org/10.1080/01457632.2015.954960.

Crystallography Open Database (COD), http://www.crystallography.net/

Daoyin, L., Zheng, W., Xiaoping, C., Malin, L. 2018. Simulation of agglomerate breakage and restructuring in shear flows: Coupled effects of shear gradient, surface energy and initial structure. *Powder Technology,* 336, 102-111. https://doi.org/10.1016/j.powtec.2018.05.051.

Dong, X., Xu, W., Zhang, Y., Leskovar, D.I. 2016. Effect of Irrigation Timing on Root Zone Soil

Temperature, Root Growth and Grain Yield and Chemical Composition in Corn. *Agronomy,* 6(2), 34. https://doi.org/10.3390/agronomy6020034.

FAO, 2016. AQUASTAT website. Water uses. Food and agriculture organization of the united nations (*FAO*). Accessed. http://www.fao.org/nr/water/aquastat/water_use/ index.stm.

Feng, J., Li, Y., Wang, W., Xue, S. 2018. Effect of optimization forms of flow path on emitter hydraulic and anti-clogging performance in drip irrigation system. *Irrigation science*, 36(1), 37-47. https://doi.org/10.1007/s00271-017-0561-9.

Freeman, W. B., Middis, J., Müller-Steinhagen, H. M. 1990. Influence of augmented surfaces and of surface finish on particulate fouling in double pipe heat exchangers. *Chemical Engineering and Processing: Process Intensification*, 27(1), 1-11. https://doi.org/10.1016/0255-2701(90)85001-K.

Hasson, D., Semiat, R., Shemer, H. 2019. A kinetic approach to desalinated water corrosion control by $CaCO_3$ films. *Desalination*, 449, 50-54. https://doi.org/10.1016/j.desal.2018.10.015.

Hasan, B. O., Nathan, G. J., Ashman, P. J., Craig, R. A., Kelso, R. M. 2012. The effects of temperature and hydrodynamics on the crystallization fouling under cross flow conditions. *Applied Thermal Engineering*, 36, 210-218. https://doi.org/10.1016/j.applthermaleng.2011.12.027.

Helalizadeh, A., Müller-Steinhagen, H., Jamialahmadi, M. 2000. Mixed salt crystallization fouling, *Chem. Eng. Process,* (39) 29-43. https://doi.org/10.1016/S0255-2701(99)00073-2.

Hou, P., Wang, T., Zhou, B., Song, P., Zeng, W., Muhammad, T., Li, Y. K. 2020. Variations in the microbial community of biofilms under different near-wall hydraulic shear stresses in agricultural irrigation systems. *Biofouling*, 36(1), 44-55. https://doi.org/10.1080/08927014.2020.1714600.

Jaffrin, M. Y., Ding, L. H., Akoum, O., Brou, A. 2004. A hydrodynamic comparison between rotating disk and vibratory dynamic filtration systems. *Journal of Membrane Science*, 242 (1-2), 155-167. https://doi.org/10.1016/j.memsci.2003.07.029.

Kaya, R., Deveci, G., Turken, T., Sengur, R., Guclu, S., Koseoglu-Imer, D. Y., Koyuncu, I. 2014. Analysis of wall shear stress on the outside-in type hollow fiber membrane modules by CFD simulation. *Desalination*, 351, 109-119. https://doi.org/10.1016/j.desal.2014.07.033.

Khoshravesh, M., Mirzaei, S. M. J., Shirazi, P., Valashedi, R. N. 2018. Evaluation of dripper clogging using magnetic water in drip irrigation. *Applied Water Science*, 8(3), 81. https://doi.org/10.1007/s13201-018-0725-7.

Korchef, A. 2019. Effect of Iron Ions on the Crystal Growth Kinetics and Microstructure of Calcium Carbonate. *Crystal Growth & Design*, 19(12), 6893-6902. https://doi.org/10.1021/acs.cgd.9b00503.

Larson, A., and Von Dreele, R. 1994. General Structure Analysis System, GSAS. Los Alamos NM: Los Alamos Laboratory.

Lee, Y. K., Won, Y. J., Yoo, J. H., Ahn, K. H., Lee, C. H. 2013. Flow analysis and fouling on the patterned membrane surface. *Journal of membrane science*, 427, 320-325. https://doi.org/10.1016/j.memsci.2012.10.010.

Li, Y. K., Pan, J., Chen, X., Xue, S., Feng, J., Muhammad, T., Zhou, B. 2019. Dynamic effects of chemical precipitates on drip irrigation system clogging using water with high sediment and salt loads. *Agricultural Water Management*, 213, 833-842. https://doi.org/10.1016/j.agwat.2018.11.021.

Li, Y. K., Song, P., Pei, Y., & Feng, J. 2015. Effects of lateral flushing on emitter clogging and biofilm components in drip irrigation systems with reclaimed water. *Irrigation Science*, 33(3), 235-245. https://doi.org/10.1007/s00271-015-0462-8.

Liu, Y., Zhou, Y., Wang, T., Pan, J., Zhou, B., Muhammad, T., Zhou, C., Li, Y. 2019. Micro-nano bubble water oxygation: synergistically improving irrigation water use efficiency, crop yield and quality. *Journal of Cleaner Production,* 222, 835-843. https://doi.org/10.1016/j.jclepro.2019.02.208.

Ma, C., Xiao, Y., Puig-Bargués, J., Shukla, M. K., Tang, X., Hou, P., Li, Y. K. 2020. Using phosphate fertilizer to reduce emitter clogging of drip fertigation systems with high salinity water. *Journal of Environmental Management*, 263, 110366. https://doi.org/10.1016/j.jenvman.2020.110366.

Ma, X., Zhao, M., Pang, Q., Zheng, M., Sun, H., Crittenden, J., Zhu, Y., Chen, Y. 2016. Development of novel $CaCO_3/Fe_2O_3$ nanorods for low temperature 1, 2-dichlorobenzene oxidation. *Applied Catalysis A: General*, 522, 70-79. http://dx.doi.org/10.1016/j.apcata.2016.04.025.

Martos, C., Coto, B., Pena, J. L., Rodriguez, R., Merino-Garcia, D., Pastor, G. 2010. Effect of precipitation procedure and detection technique on particle size distribution of $CaCO_3$. *Journal of Crystal Growth*, 312(19), 2756-2763. https://doi.org/10.1016/j.jcrysgro.2010.06.006.

Mejri, W., Korchef, A., Tlili, M., Ben Amor, M. 2014. Effects of temperature on precipitation kinetics and microstructure of calcium carbonate in the presence of magnesium and sulphate ions. *Desalination and Water Treatment*, 52(25-27), 4863-4870. https://doi.org/10.1080/19443994.2013.808813.

Mhadhbi, M., Khitouni, M., Escoda, L., Sunol, J. J., Dammak, M. 2010. Characterization of mechanically alloyed nanocrystalline Fe (Al): crystallite size and dislocation density. *Journal of Nanomaterials*, https://doi.org/10.1155/2010/712407.

Mwaba, M. G., Rindt, C. C. M., Van Steenhoven, A. A., Vorstman, M. A. G. 2006. Experimental investigation of $CaSO_4$ crystallization on a flat plate. *Heat transfer engineering*, 27(3), 42-54. https://doi.org/10.1080/01457630500458187.

Nancollas, G. H., Reddy, M. M. 1971. The crystallization of calcium carbonate. II. Calcite growth mechanism. *Journal of colloid and interface science*, 37(4), 824-830. https://doi.org/10.1016/0021-9797(71)90363-8.

Ngan, W. Y., & Habimana, O. 2020. From farm-scale to lab-scale: The characterization of engineered irrigation water distribution system biofilm models using an artificial freshwater source. *Science of The Total Environment*, 698, 134025. https://doi.org/10.1016/j.scitotenv.2019.134025.

Paz, C., Suárez, E., Eirís, A., Porteiro, J. 2012. Experimental evaluation of the critical local wall shear stress around cylindrical probes fouled by diesel exhaust gases. *Experimental thermal and fluid science*, 38, 85-93. https://doi.org/10.1016/j.expthermflusci.2011.11.011.

Pääkkönen, T. M., Riihimäki, M., Simonson, C. J., Muurinen, E., Keiski, R. L. 2012. Crystallization fouling of $CaCO_3$–Analysis of experimental thermal resistance and its uncertainty. *International Journal of Heat and Mass Transfer*, 55(23-24), 6927-6937.

https://doi.org/10.1016/j.ijheatmasstransfer.2012.07.006.

Peragón, J. M., Pérez-Latorre, F. J., Delgado, A. 2017. A GIS-based tool for integrated management of clogging risk and nitrogen fertilization in drip irrigation. *Agricultural Water Management*, 184, 86-95. https://doi.org/10.1016/j.agwat.2017.01.007.

Puig-Bargués, J., & Lamm, F. R. 2013. Effect of flushing velocity and flushing duration on sediment transport in microirrigation driplines. *Transactions of the ASABE*, 56(5), 1821-1828. https://doi: 10.13031/trans.56.10293.

Qi, W. H., Wang, M. P. 2005. Size and shape dependent lattice parameters of metallic nanoparticles. *Journal of Nanoparticle Research*, 7(1), 51-57. https://doi.org/10.1007/s11051-004-7771-9.

Rochex, A., Godon, J. J., Bernet, N., Escudié, R. 2008. Role of shear stress on composition, diversity and dynamics of biofilm bacterial communities. *Water Research,* 42(20), 4915-4922. https://doi.org/10.1016/j.watres.2008.09.015.

Rodriguez-Blanco, J. D., Shaw, S., Bots, P., Roncal-Herrero, T., Benning, L. G. 2012. The role of pH and Mg on the stability and crystallization of amorphous calcium carbonate. *Journal of Alloys and Compounds*, 536, S477-S479. https://doi.org/10.1016/j.jallcom.2011.11.057.

Sheng, J., Welzel, U., Mittemeijer, E. J. 2010. Nonmonotonic crystallite-size dependence of the lattice parameter of nanocrystalline nickel. *Applied Physics Letters*, 97(15), 153109. https://doi.org/10.1063/1.3500827.

Song, P., Feng, G., Brooks, J., Zhou, B., Zhou, H., Zhao, Z., & Li, Y. 2019. Environmental risk of chlorine-controlled clogging in drip irrigation system using reclaimed water: the perspective of soil health. *Journal of Cleaner Production*, 232, 1452-1464. https://doi.org/10.1016/j.jclepro.2019.06.050.

Sonwai, S., Mackley, M. R. 2006. The effect of shear on the crystallization of cocoa butter. *Journal of the American Oil Chemists' Society*, 83(7), 583-596. https://doi.org/10.1007/s11746-006-1243-6.

Soos, M., Moussa, A. S., Ehrl, L., Sefcik, J., Wu, H., & Morbidelli, M. 2008. Effect of shear rate on aggregate size and morphology investigated under turbulent conditions in stirred tank.

Journal of Colloid and Interface Science, 319(2), 577-589. https://doi.org/10.1016/j.jcis.2007.12.005.

Wang, L. C., Li, S. F., Wang, L. B., Cui, K., Zhang, Q. L., Liu, H. B., Li, G. 2016. Relationships between the characteristics of $CaCO_3$ fouling and the flow velocity in smooth tube. *Experimental Thermal and Fluid Science*, 74, 143-159. https://doi.org/10.1016/j.expthermflusci.2015.12.001.

Xiao, Y., Sawicka, B., Liu, Y., Zhou, B., Hou, P., Li, Y. 2020. Visualizing the macroscale spatial distributions of biofilms in complex flow channels using industrial computed tomography. *Biofouling*, 36(2), 115-125. https://doi.org/10.1080/08927014.2020.1728260.

Yang, D., Hrymak, A. N., Kamal, M. R. 2011. Crystal Morphology of hydrogenated castor oil in the crystallization of oil-in-water emulsions: Part II. Effect of shear. *Industrial & engineering chemistry research*, 50(20), 11594-11600. https://doi.org/10.1021/ie1025985.

Zhang, C., Li, X., Kang, Y., & Wang, X. 2019. Salt leaching and response of Dianthus chinensis L. to saline water drip-irrigation in two coastal saline soils. *Agricultural Water Management*, 218, 8-16. https://doi.org/10.1016/j.agwat.2019.03.020.

Zhang, Y., Li, X., Li, K., Lian, H., Shang, M., Lin, J. 2015. Crystal-site engineering control for the reduction of Eu^{3+} to Eu^{2+} in $CaYAlO_4$: structure refinement and tunable emission properties. *ACS Applied Materials & Interfaces*, 7(4), 2715-2725. https://doi.org/10.1021/am508859c.

Zhangzhong, L., Yang, P., Zhen, W., Zhang, X., Wang, C. 2019. A kinetic model for the chemical clogging of drip irrigation system using saline water. *Agricultural Water Management*, 223, 105696. https://doi.org/10.1016/j.agwat.2019.105696.

Zhangzhong, L., Yang, P., Zheng, W., Wang, C., Zhang, C., Niu, M. 2018. Effects of drip irrigation models on chemical clogging under saline water use in Hetao District, China. *Water*, 10(3), 345. https://doi.org/10.3390/w10030345.

Zhangzhong, L.L., Yang, P.L., Ren, S.M., Li, Y.K., Liu, Y., Xia, Y.H. 2016. Chemical clogging of emitters and evaluation of their suitability for saline water drip irrigation. *Irrigation and Drainage*, 65 (4), 439–450. https://doi.org/10.1002/ird.1972.

Zhou, B., Li, Y., Song, P., Zhou, Y., Yu, Y., & Bralts, V. 2017. Anti-clogging evaluation for drip irrigation emitters using reclaimed water. *Irrigation Science*, 35(3), 181-192. https://doi.org/10.1007/s00271-016-0530-8.

Captions for Tables in the Paper

Table 1; Effects of near-wall shear stress, temperature and ions on content of $CaCO_3$ fouling dry weight, calcite and aragonite.

Table 1. Effects of near-wall shear stress, temperature and ions on content of $CaCO_3$ fouling dry weight, calcite and aragonite.

Variables	Fouling dry weight		Calcite		Aragonite	
	MS	*F (p value)*	*MS*	*F (p value)*	*MS*	*F (p value)*
S	2.75	835.6*	1.07	478.7*	0.34	259.2$^{n.s.}$
T	1.64	409.8*	0.85	306.1*	0.56	601.2$^{n.s.}$
I	2.29	191.0*	0.54	250.3*	0.46	977.7*
S × T	0.86	88.9*	0.48	44.5*	0.21	22.48*
S × I	0.58	38.0*	0.53	30.6*	0.36	98.7*
T× I	0.43	17.3*	0.47	15.5*	0.22	197.6*
S × T × I	0.23	2.15$^{n.s.}$	0.14	2.19$^{n.s.}$	0.54	12.9$^{n.s.}$

Note; S, shear stress; T, temperature; I, ions and MS, mean square error. (not significant, n.s, p >0.05; * p< 0.05)

Captions for Figures in the Paper

Fig. 1 Schematic layout of annular reactor (AR) used for $CaCO_3$ fouling.

Fig 2. Dynamic variation of $CaCO_3$ fouling as function of operation time in different treatments.

Fig 3. XRD diffraction pattern, Rietveld refinement results and variation of total content of calcite and aragonite.

Fig 4. Variation of fouling crystals mean sizes among shear stress in each treatment.

Fig. 5 Variation in apparent morphologies of $CaCO_3$ fouling in different treatments.

Fig 6. Variation of crystal unit cell-volume (Cv) and lattice parameters (*a*-axis, *b*-axis and *c*-axis) in different treatments.

Fig. 7. Structural equation modelling analysis (SEMA), showing the pathway regularity of shear stress, temperature and impurity ions on $CaCO_3$ fouling.

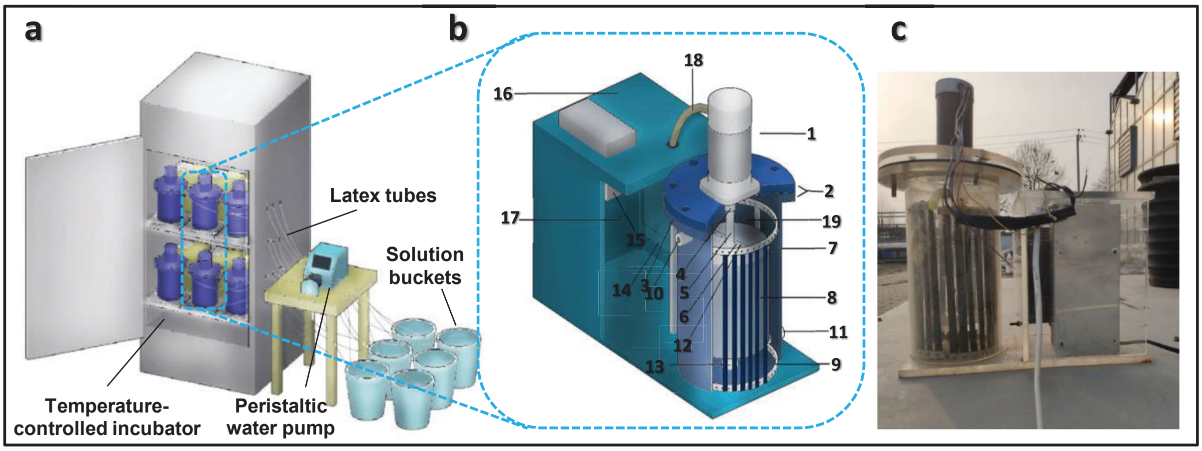

Fig. 1 Schematic layout of annular reactor (AR) used for fouling; a, Temperature-controlled complete apparatus; b, Single AR; and c, Actual condition of AR. 1, Power motor; 2, Flange joint plates; 3, Gasket seal; 4, Connecting bearing; 5, Motor shaft; 6, Steel disc; 7, Exterior cylinder; 8, Interior cylinder; 9, Sample frame; 10, Water outlet; 11, Water inlet; 12, Bolts; 13, Fixed bearing; 14, Potential transformer; 15, Servo motor; 16, Distribution box; 17, Heat emission hole; 18, Electric wire; 19, Sample sink.

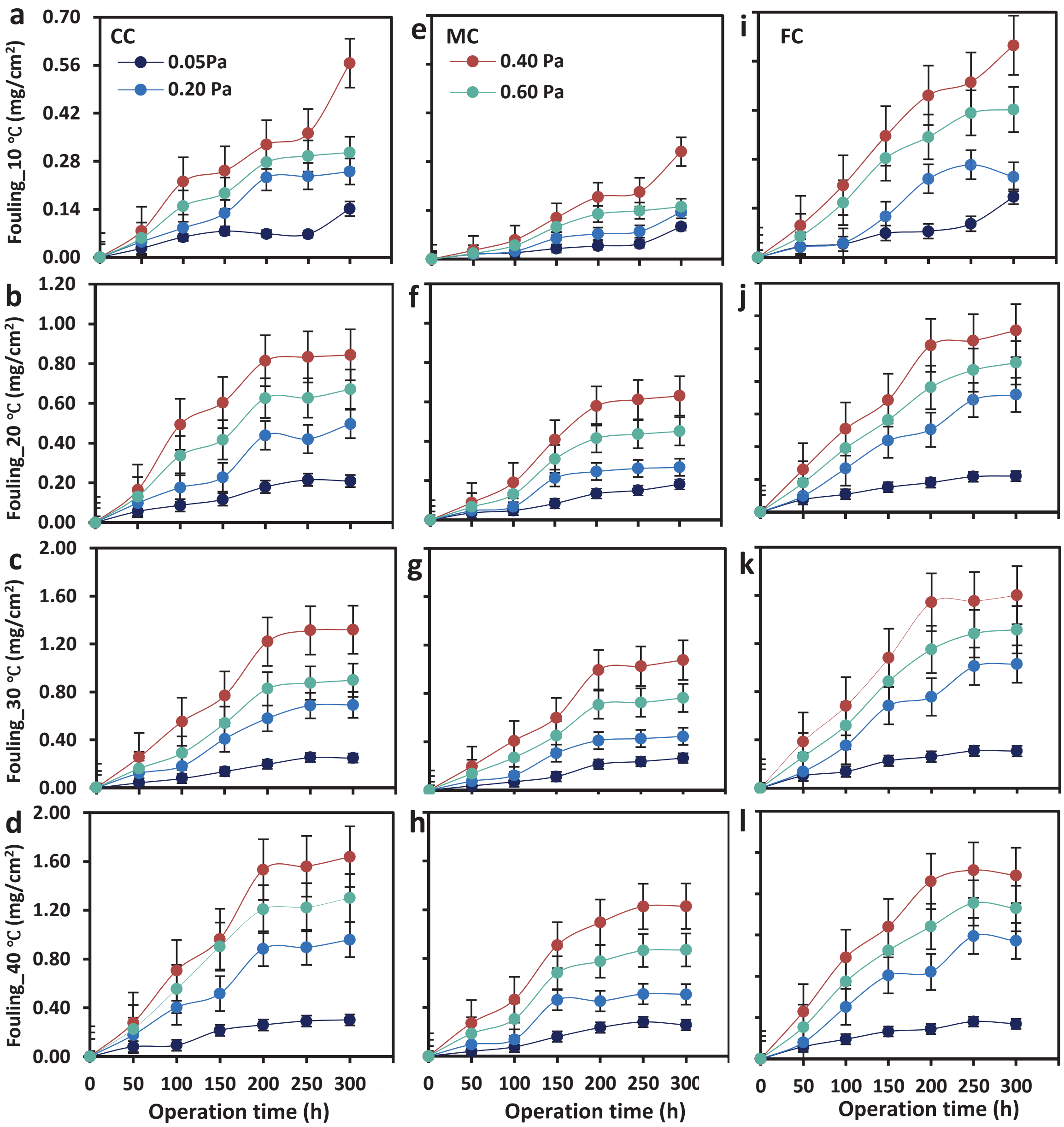

19

20 Fig 2. Dynamic variation of $CaCO_3$ fouling as function of operation time in different treatments; CC (a, b, c,

21 d); MC (e, f, g, h); FC (i, j, k, l). and temperature (10, 20, 30, and 40 ℃).

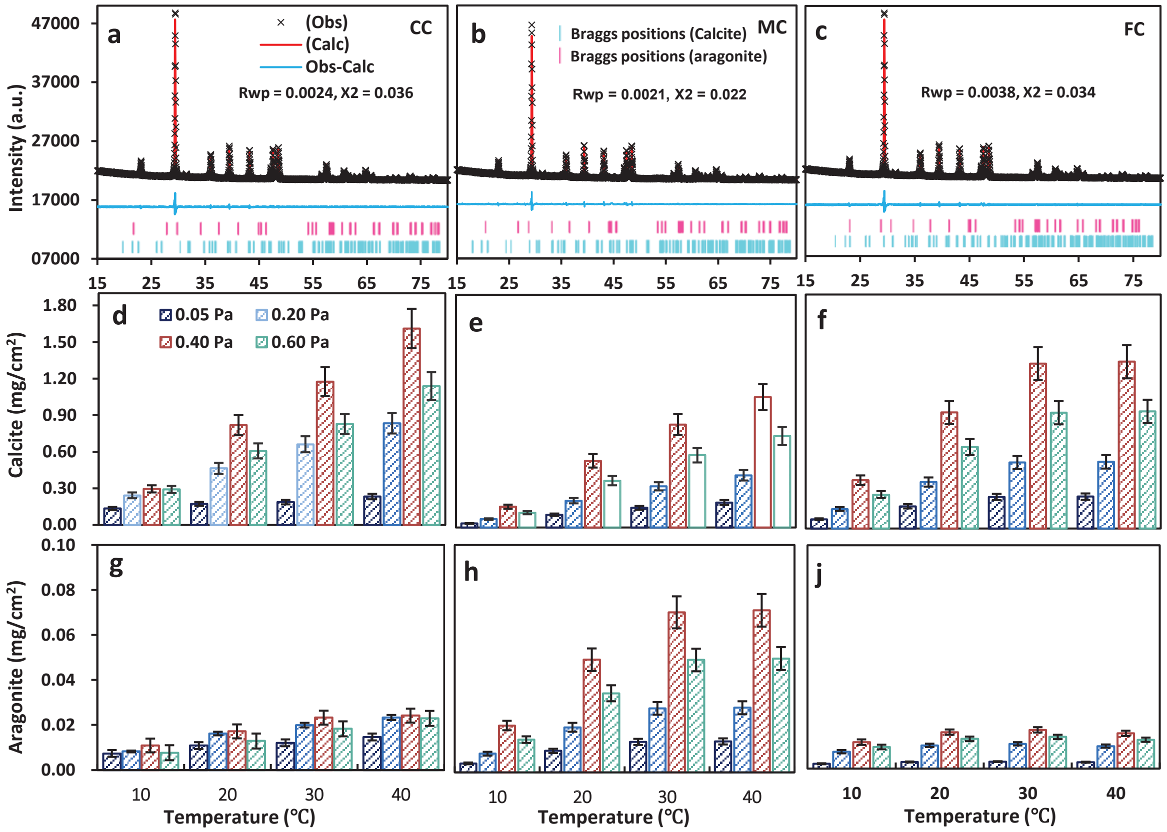

Fig 3. XRD diffraction pattern, Rietveld refinement results and variation of total content of calcite and aragonite; Rietveld refinement results (a, b, c); the total quantity of calcite (d, e, f); and total quantity of aragonite (g, h, i); in ions treatments CC; MC and FC. The X-ray diffraction and Rietveld refinement results presented here are taken as an example obtained at shear stress of 0.40 Pa and 40 °C.

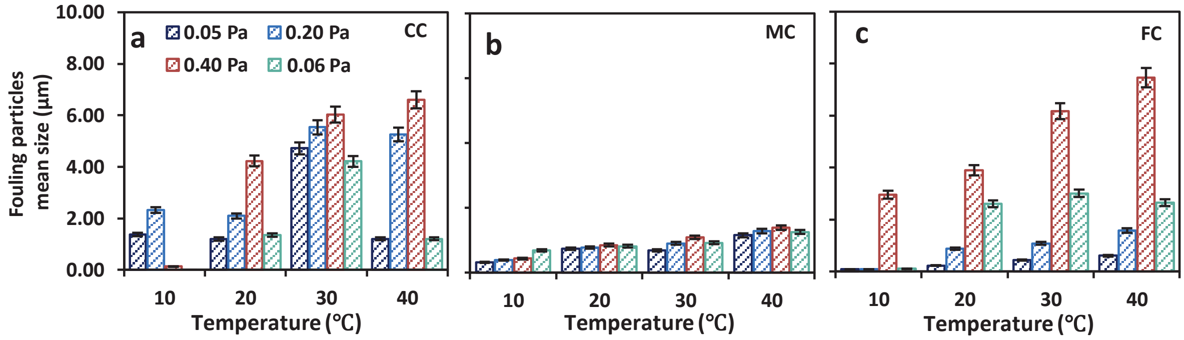

Fig 4. Variation of fouling crystals mean sizes among shear stress in each treatment; CC (a); MC (b), and FC (c).

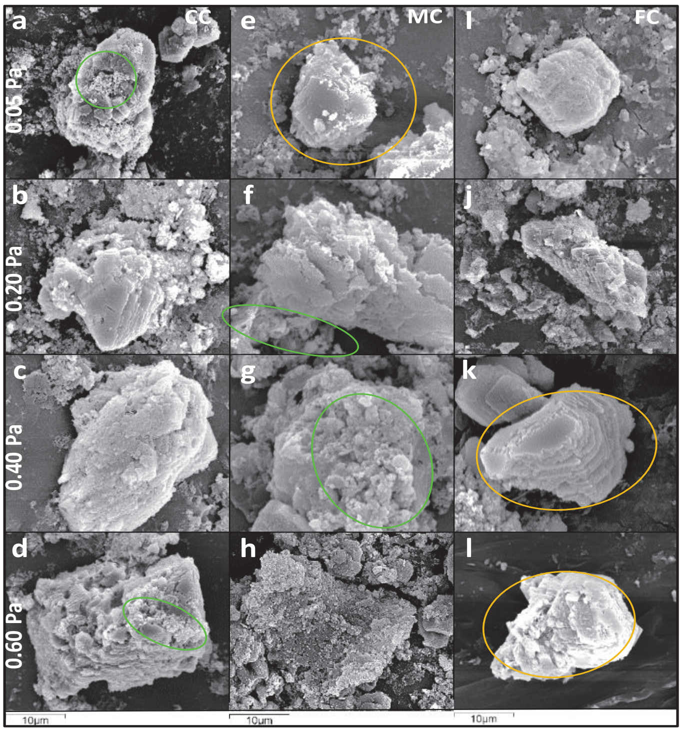

Fig. 5 Variation in apparent morphologies of $CaCO_3$ fouling in different treatments; CC; (a, b, c, d); MC (e, f, g, h); FC (i, j, k, l), and shear stress 0.05, 0.20, 0.40, and 0.60 Pa. The orange and green circles indicate the presence of calcite and aragonite.

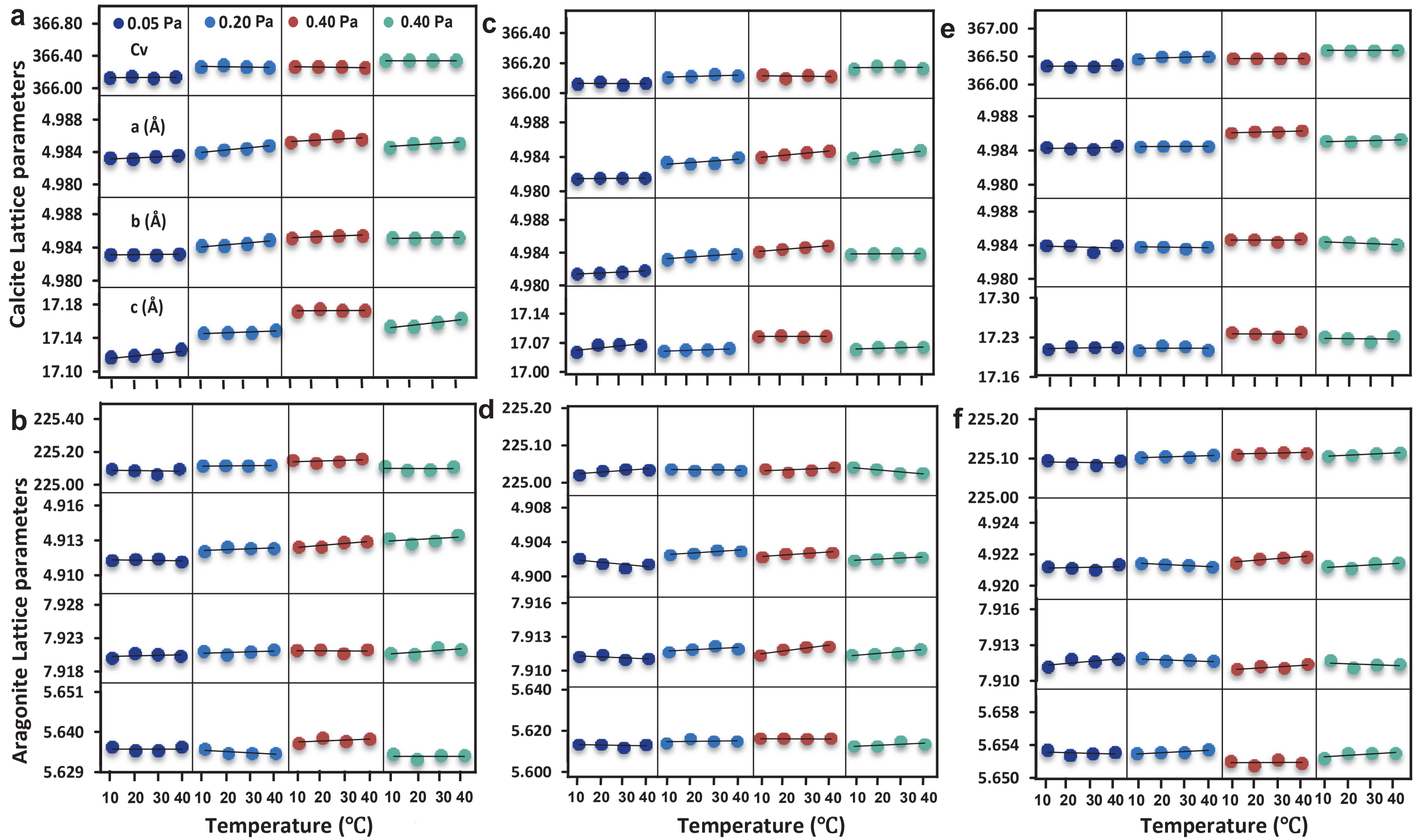

Fig 6. Variation of crystal unit cell-volume (Cv) and lattice parameters (*a-axis*, *b-axis* and *c-axis*) in different treatments; CC (a, b); MC (c, d); FC (e, f).

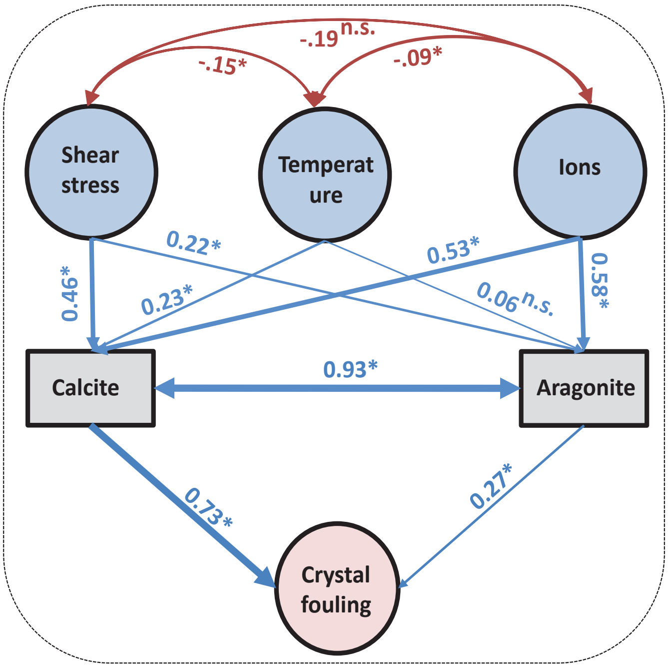

Fig. 7. Structural equation modelling analysis (SEMA), showing the pathway regularity of shear stress, temperature and impurity ions on $CaCO_3$ fouling; Note; χ^2= 16.972 (p = 0.001), Degrees of freedom (df) = 3, Root mean square error of approximation (*RMSEA*) = 0.038, with probability of a close fit = 0.02. Blue and red arrows represent positive and negative relationship, Numbers on the arrows are standard path coefficients (β). Width of arrows indicate the strength of relationship. n.s p >0.05; * p< 0.05.